ACS APPLIED MATERIALS & INTERFACES

www.acsami.org

Research Article

Structural and Chemical Transformations of Zinc Oxide Ultrathin Films on Pd(111) Surfaces

Junxian Gao, Kaustubh J. Sawant, Jeffrey T. Miller, Zhenhua Zeng,* Dmitry Zemlyanov,* and Jeffrey P. Greeley*

Cite This: https://doi.org/10.1021/acsami.1c07510

Read Online

ACCESS | Metrics & More | Article Recommendations | Supporting Information

ABSTRACT: Structural and chemical transformations of ultrathin oxide films on transition metals lie at the heart of many complex phenomena in heterogeneous catalysis, such as the strong metal−support interaction (SMSI). However, there is limited atomic-scale understanding of these transformations, especially for irreducible oxides such as ZnO. Here, by combining density functional theory calculations and surface science techniques, including scanning tunneling microscopy, X-ray photoelectron spectroscopy, high-resolution electron energy loss spectroscopy, and low-energy electron diffraction, we investigated the interfacial interaction of well-defined ultrathin ZnO_xH_y films on Pd(111) under varying gas-phase conditions [ultrahigh vacuum (UHV), 5×10^{-7} mbar of O_2, and a D_2/O_2 mixture] to shed light on the SMSI effect of irreducible oxides. Sequential treatment of submonolayer zinc oxide films in a D_2/O_2 mixture (1:4) at 550 K evoked reversible structural transformations from a bilayer to a monolayer and further to a Pd−Zn near-surface alloy, demonstrating that zinc oxide, as an irreducible oxide, can spread on metal surfaces and show an SMSI-like behavior in the presence of hydrogen. A mixed canonical−grand canonical phase diagram was developed to bridge the gap between UHV conditions and true SMSI environments, revealing that, in addition to surface alloy formation, certain ZnO_xH_y films with stoichiometries that do not exist in bulk are stabilized by Pd in the presence of hydrogen. Based on the combined theoretical and experimental observations, we propose that SMSI metal nanoparticle encapsulation for irreducible oxide supports such as ZnO involves both surface (hydroxy)oxide and surface alloy formation, depending on the environmental conditions.

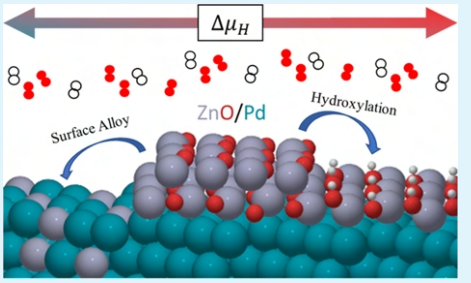

KEYWORDS: *strong metal−support interaction, ZnO_x/Pd(111), irreducible oxide, hydroxylation, Pd−Zn alloy, scanning tunneling microscopy, density functional calculations*

1. INTRODUCTION

Catalytic activity of an oxide-supported transition-metal catalyst is greatly influenced by the nature of metal−oxide interactions. The oxide supports are known to interact with the nanoparticles in highly complex and non-intuitive ways that fundamentally alter the catalytic properties of the system. Although such effects have been studied for decades, the atomic-level interactions between the metal and the support and the impact that these interactions have on catalytic properties are not well understood. In particular, the strong metal−support interaction (SMSI) was first investigated 40 years ago by Tauster et al.[1] It was observed that the ability of titanium oxide-supported metal nanoparticles to bind adsorbates was considerably suppressed after heating at 500 °C in a reducing atmosphere. Electron microscopy has confirmed the existence of an encapsulating layer consisting of modified support oxides on top of the metal nanoparticles in various related cases.[2,3] This encapsulation model is consistent with suppressed adsorption, but the model does not exclude other possible SMSI-related effects, including alloying and charge transfer. Although historically associated with coverage and deactivation of catalytic sites, recent developments suggest that, in certain circumstances, the SMSI oxide can modify catalytic active sites, resulting in improved catalytic properties.[4]

Despite many studies related to the electronic and geometric changes in the metal nanoparticles by the SMSI overlayer and the impact of these effects on catalytic performance, the mechanism of the SMSI remains elusive. Reduction in pure or diluted H_2 is usually required for the formation of SMSI overlayers.[5] The SMSI overlayer has a stoichiometry different from that of corresponding bulk phases, and the metal cation in the overlayer exhibits a lower oxidation state than that in the oxide supports, as observed using X-ray photoelectron spectroscopy (XPS).[6,7] Thus, the oxide support must be partially reduced before migrating over the metal nanoparticle surface,[8] either through reacting with H_2 and forming H_2O or decomposing and desorbing O_2 in the vacuum. The former

Received: April 23, 2021
Accepted: July 1, 2021

pathway also requires reactivity of the metal toward H_2 activation. The discovery of such partially reduced oxide overlayers has been interpreted to signify that only reducible oxides might show SMSI, where the metal cations can show multiple oxidation states; and diffusive MO_x species (M: Ti,[5] Nb,[9] Mn,[10] Fe,[7] where x is smaller than the bulk stoichiometry number) are necessary to enable migration of oxide supports onto the metal surface.

Recently, ZnO, a non-reducible oxide, has also been reported to exhibit an SMSI effect in Cu/ZnO-based catalysts during methanol synthesis.[11,12] M. Behrens et al. observed a disordered ZnO_x overlayer on a $Cu/ZnO/Al_2O_3$ catalyst at low partial pressure of hydrogen using high-resolution transmission electron microscopy.[13] T. Lunkenbein et al. reported that the ZnO_x overlayer on a Cu nanoparticle transformed from graphite-like ZnO_x to rocksalt ZnO and, eventually, wurtzite ZnO upon electron beam exposure.[14] Further, a depolarized graphite-like overlayer structure was predicted[15] and observed on ZnO/Ag(111)[16] and ZnO/Pd(111)[17] inverse model catalysts.[14] Infrared spectroscopy (IR) and theoretical analysis done by Schott et al. suggested that the ZnO overlayer showed different chemical properties compared to those of the wurtzite bulk structure and seemed to be partially reduced to a less strongly oxidized $Zn^{\delta+}$ state through SMSI.[18] These findings indicate that the structure of ZnO overlayers on metal surfaces is highly dynamic and that SMSI may be observed even on non-reducible oxides.

In the present study, the atomic-level features of the dynamic structural transformations of well-defined ZnO_xH_y ultrathin films on Pd(111) were investigated through surface science. Then, the extrapolation to the general thermodynamic driving forces of SMSI behavior was enabled through first-principles phase diagrams. We chose the current system because of the promising applications of Pd/ZnO catalysts to methanol synthesis and steam reforming of methanol.[19−21] Introduction of small amounts of hydrogen under ultrahigh vacuum (UHV) conditions resulted in the reduction of ZnO to surface ZnO_x and further to a Pd−Zn near-surface alloy. By combining these observations with density functional theory (DFT) calculations and a mixed canonical−grand canonical phase diagram, we deduced those small ensembles of ZnO on the surface are susceptible to reduction and will subsequently form subsurface alloys. The DFT calculations further demonstrate that certain ultrathin ZnO_xH_y films which are metastable in UHV can, in fact, become stable under SMSI conditions with a higher pressure of hydrogen. From these results, we propose that even irreducible oxides, such as ZnO, can exhibit SMSI-like behavior via favorable formation of ZnO_xH_y films or near-surface alloys, with a dependence on the gas-phase conditions that drives the migration of Zn over metal particles.

2. METHODS

2.1. Experimental Methods. All experiments were carried out in an Omicron surface analysis cluster consisting of two main UHV chambers. The preparation chamber (base pressure is $\sim 6 \times 10^{-10}$ mbar) is equipped with gas manifolds for chemical vapor deposition and a Zn evaporator for physical vapor deposition. The analysis chamber (base pressure is $\sim 6 \times 10^{-11}$ mbar) is equipped with room temperature Omicron scanning tunneling microscopy (STM), XPS, high-resolution electron energy loss spectroscopy (HREELS), and low energy electron diffraction (LEED).

The Pd(111) single crystal was cleaned by cycles of Ar^+ sputtering, annealing in 1×10^{-6} mbar of O_2, and annealing in UHV. The cleanliness of the Pd(111) surface was monitored by XPS. ZnO films on Pd(111) were prepared by exposing the surface to diethylzinc at room temperature or by oxidative deposition of metallic Zn in 1×10^{-7} mbar of O_2, followed by post-oxidation in O_2 or a D_2/O_2 mixture at 550 K for 10 min. D_2 was used instead of H_2 throughout our experiments so that we could distinguish the external (intentional exposure) and internal (residual gas) sources of hydrogen by HREELS. The partial pressure of D_2 was calculated by taking into consideration the ionization parameter of the gas. The coverage of ZnO on Pd was controlled by diethylzinc (or metallic Zn) exposure and was calculated using the area of Zn $2p_{3/2}$ and Pd $3d_{5/2}$ XPS peaks under the assumption of a non-attenuating ZnO adlayer.[22] This approach has been well validated and is described in detail elsewhere.[23,24]

After ZnO preparation, the sample stage was cooled rapidly, and the sample was then transferred within 1−2 min to the analysis chamber for characterization by HREELS, STM, LEED, and XPS. HREELS measurements were performed using an ELS 5000 (LK Technologies). The scattered electrons were collected in specular direction with primary electron beam energy of 5 eV. The full width at half-maximum (fwhm) of the elastic peak of the sample was between 2.5 and 3.0 meV (equivalent to 20−24 cm^{-1}). The intensity of energy loss was normalized to the intensity of the elastic peak.

XPS data were collected using a non-monochromatic Mg Kα X-ray source at an incidence angle of 45°. The emitted photoelectrons were collected using an Omicron EAC 125 analyzer and an Omicron EAC 2000 analyzer controller at a photoemission angle of 45° with respect to the surface normal. Binding energy values refer to the Fermi edge, and the energy scale was calibrated using Au $4f_{7/2}$ at 84.0 eV and Cu $2p_{3/2}$ at 932.67 eV. Since the sample was conductive and ground, no charge correction was necessary. The Pd $3d_{5/2}$ peak for the clean Pd(111) surface was observed at 335.2 eV. XPS data were analyzed using CasaXPS software.

STM imaging was performed at a constant current mode at room temperature with tungsten tips, which were prepared by electrochemical etching of 0.25 mm (or 0.175 mm) tungsten wires and cleaned by electron bombardment in UHV. The bias voltage varied from +0.8 to +1.5 V with tunneling current ranging from 0.5 to 1.0 nA. STM images were analyzed using WSxM software.[25]

2.2. Computational Methods. *2.2.1. Electronic Structure Calculations.* Periodic DFT calculations were performed as implemented in Vienna *ab initio* simulation package.[26,27] The core electrons were modeled using projector augmented wave (PAW) potentials.[28] The generalized gradient approximation developed by Perdew−Burke−Ernzerhof was used as the exchange−correlation functional.[29] The energy cutoff for the planewave basis set was 500 eV. The Brillouin zone was sampled using Monkhorst−Pack. A large number of unique unit cells were studied, and we ensured in all cases that the lattice constant times number of K points was 30 Å. The substrates had four metal layers with the bottom two constrained. A single K point and an orthorhombic unit cell was used for calculations involving gas phase species. The STM images were simulated using Atomic Simulation Environment modules[30] and GPAW.[31]

2.2.2. Geometric Structures. The ultrathin film structures were primarily made by cutting along different terminations of bulk structures. Since zinc has only one oxidation state (+2), there are only two stable bulk structures—ZnO and $Zn(OH)_2$. In order to study stoichiometries that do not exist in bulk, terminations from stable bulk crystalline polymorphs, such as TiO_2, V_2O_3, LiOH, and NiOOH, were used, where the cation was replaced with Zn. Experimental STM images of the films were also compared to DFT-simulated STM images to refine the proposed film structures. In addition, Pd is known to form an alloy with Zn under reducing conditions.[32] Under highly oxidizing conditions, however, Pd is known to dissolve oxygen at the surface.[33−36] Therefore, both Pd−Zn surface alloys and PdO films on Pd were included in the analysis. To minimize strain in ZnO_xH_y overlayers, ZnO_xH_y/Pd(111) interfaces were modeled using a Morié pattern strategy developed in our previous work.[37]

2.2.3. Ab Initio Phase Diagrams. *Ab initio* thermodynamic phase diagrams allow the investigation of thermodynamic conditions under

https://doi.org/10.1021/acsami.1c07510
ACS Appl. Mater. Interfaces XXXX, XXX, XXX−XXX

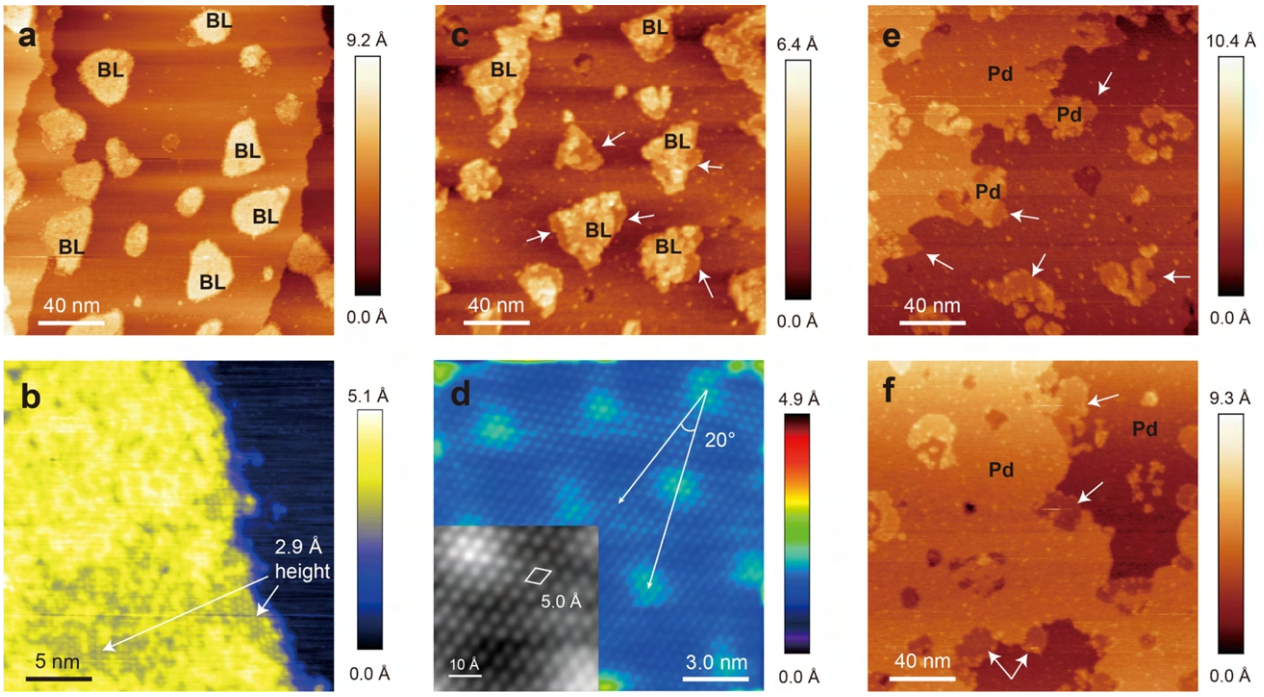

Figure 1. STM images of 0.32 ML ZnO_x/Pd(111) with the structural transformation from bilayer ZnO islands to a Pd−Zn alloy through the monolayer "5Å-ZnO_x" structure. (a) Fresh 0.32 ML ZnO_x/Pd(111) surface with dominant bilayer islands (labeled as BL). (b) Magnified image of a bilayer island. The white arrows indicate the atomically resolved regions with 5 Å periodicity and 2.9 Å apparent height. (c) Surface after sequential treatments in a 5×10^{-7} mbar D_2/O_2 (1:4) mixture at 550 K for 10 min. (d) Atomic resolution image of the monolayer "5Å-ZnO_x" structure [also denoted (18×18) R20° based on the superlattice]. The two arrows show the rotated 20° angle between the atomic periodicity and superstructure periodicity. The rhombus in the inset indicates the atomic unit cell with a side length of 5.0 Å. (e,f) Surface after second and third treatments in a 5×10^{-7} mbar D_2/O_2 (1:4) mixture at 550 K for 10 and 20 min, respectively. The white arrows indicate the monolayer "5Å-ZnO_x" structure.

which ultrathin metal oxide films may be stabilized. The pressure and temperature dependence of the thermodynamic stability of surfaces can be understood through the formulation developed by Reuter and Scheffler,[38] wherein the environment-dependent interfacial energies of many different surface phases are compared to determine which phase is the thermodynamic ground state under the given conditions. This formulation assumes that the catalyst surface is in equilibrium with the gas phase and bulk reservoirs within the grand canonical ensemble. Equation 1 defines the free energy of the surface phase with respect to the various bulk reservoirs under conditions given by the gas phase chemical potentials. Normalizing eq 1 by area will give the surface formation energy. In this analysis, ZnO and Pd are identified as the bulk reservoirs; while, the potentials of O and H are independent variables and account for the temperature and pressure dependence.

$$\Omega = E^{\mathrm{DFT}}_{\mathrm{Zn}_a\mathrm{O}_b\mathrm{H}_c/\mathrm{Pd}(111)} - E^{\mathrm{DFT}}_{\mathrm{bare\ Pd}(111)} - aE^{\mathrm{DFT}}_{\mathrm{ZnO\ bulk}} - c\mu_{\mathrm{H}}(T, P) - (b - a)\mu_{\mathrm{o}}(T, P) \quad (1)$$

This thermodynamic formalism is descriptive of realistic SMSI systems, wherein a metal nanoparticle is supported on an oxide. In this case, both the support and the nanoparticle are large enough to be considered as thermodynamic reservoirs, as discussed above. However, in the case of natively grown ultrathin oxides, as are observed in the surface science context with films deposited on single crystal metal substrates, an infinite metal oxide (ZnO) reservoir does not exist, and it is therefore difficult to estimate the chemical potential of Zn. Hence, a pseudo-canonical ensemble must be used, where Zn is represented by the number of Zn atoms and not the Zn chemical potential. The definition of the free energy $\Lambda(T, A, \mu_{\mathrm{O}}, \mu_{\mathrm{H}}, \mu_{\mathrm{Pd}}, N_{\mathrm{Zn}})$ is given by eq 2:

$$\Lambda = U - TS - N_{\mathrm{O}}\mu_{\mathrm{O}} - N_{\mathrm{H}}\mu_{\mathrm{H}} - N_{\mathrm{Pd}}\mu_{\mathrm{Pd}} \quad (2)$$

$$\frac{\Lambda}{A} = \lambda_{\mathrm{A}} = \gamma + \mu_{\mathrm{Zn}}\eta_{\mathrm{Zn}};\ \eta_{\mathrm{Zn}} = \frac{N_{\mathrm{Zn}}}{A} \quad (3)$$

where γ is the interfacial tension. The derivation of surface free energy (λ_A) (eq 3), which is plotted against the ratio of Zn per surface area, referenced to a Pd(111) slab, and the details of the hydrogen and oxygen chemical potentials are discussed in the Supporting Information. The resulting phase diagram is a classic convex hull, where the stable structures have positive second derivatives. The thermodynamically stable phases can thus be identified for the various Zn coverages, and these can be directly compared to experimental surface science measurements. Although the above equation is derived for the $Zn_aO_bH_c$/Pd system, it can easily be generalized to other systems with a varying number of gaseous or bulk species, and the current method developed is therefore appropriate for general comparisons of results with experiments where ultrathin films are grown on substrates.

3. RESULTS AND DISCUSSION

3.1. Reversible Structural Transformation from ZnO Islands to Near-Surface Alloys through a "5Å-ZnO_x" Monolayer Structure. We begin our study of the ZnO/Pd system by preparing submonolayer ZnO films on Pd(111) under three different gas-phase conditions and at two different temperatures. Isolated islands with irregular shapes are formed (STM image in Figure 1a) by deposition of diethylzinc at room temperature, annealing in UHV at 423 K, and post-oxidation in 5×10^{-7} mbar of O_2 at 550 K for 10 min. The average apparent height of these islands is 3.4 ± 0.2 Å, suggesting that there are two layers of Zn−O. The magnified image of a bilayer island in Figure 1b indicates a non-uniformity of the island, where some regions are higher and appear amorphous; while, other areas are lower, and an ordered assembly of atoms can be distinguished. Histograms in Figure S1 in the Supporting Information show that the average

https://doi.org/10.1021/acsami.1c07510
ACS Appl. Mater. Interfaces XXXX, XXX, XXX−XXX

heights of the amorphous and ordered regions are 3.9 and 2.9 Å, respectively. HREELS detects a ν(O−H) vibration as a sharp loss peak at 3625 cm^{-1} (Figure 2, black line), which is

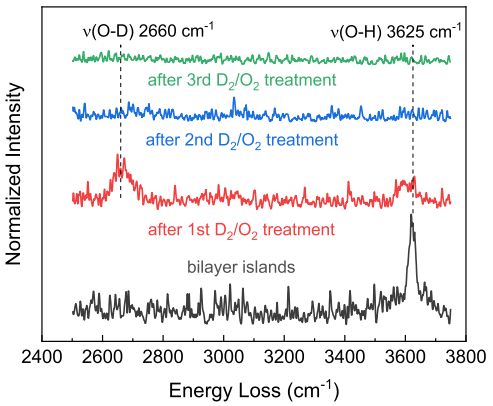

Figure 2. HREELS analysis of the as-prepared 0.32 ML ZnO_x/Pd(111) surface with dominant bilayer ZnO islands and the surfaces after three sequential treatments in a D_2/O_2 (1:4) mixture at 550 K for 10, 10, and 20 min, respectively. The intensity of the energy loss peaks was normalized to the intensity of the corresponding elastic peaks.

indicative of hydroxyl species, and suggesting that the 1.0 Å height difference can be attributed to hydroxyl species on the surface of ZnO islands. A small fwhm of the ν(O−H) peak (fwhm = 34 cm^{-1}) can be explained by a homogenous chemical environment of the hydroxyl species. It should be noted that hydroxylated zinc oxide films have also been observed on Pt(111) in the absence of hydrogen.[39] There are, in turn, three possible hydrogen sources, which could result in hydroxyl species formation, including (i) residual hydrogen in the UHV chamber, (ii) hydrocarbons from diethylzinc decomposition, and (iii) dissolved hydrogen stored in the Pd subsurface and bulk.[40] The coverage of Zn is a 0.32 monolayer (ML), as calculated from XPS. Taken together, the data support assignment of the structure to partially hydroxylated, two-layer ZnO islands (labeled as BL in the STM images).

Dynamic change of the bilayer ZnO was investigated by three sequential treatments at 550 K in 5×10^{-7} mbar of a D_2/O_2 (1:4) mixture, an intermediate between the oxidative (pure oxygen) and reducing (UHV or pure hydrogen) conditions. After the first 10 min of treatment, darker, step-like, narrow terraces started to grow out of the bilayer islands, as indicated by the white arrows in Figure 1c. The apparent height of this new structure is 1.4 ± 0.1 Å, suggesting a spreading of ZnO from a bilayer to a monolayer. The magnified image with atomic resolution reveals a 5.0 Å atomic periodicity and a 49.5 Å superlattice on this monolayer structure (Figure 1d); the atomic structure of this monolayer film (labeled as "5Å-ZnO_x") will be discussed later. The first appearance of monolayer "5Å-ZnO_x" at the perimeter implies that the transition occurs first at the metal−oxide boundary and gradually propagates into the inner area of the ZnO bilayer islands.

Treating the sample for 10 additional minutes under the same conditions led to the conversion of the remaining bilayer islands to the monolayer structure (Figure 1e). The direction of Pd monoatomic steps remained unchanged, but the shape was distorted compared to that in Figure 1a. Also, the surface coverage of oxide decreased significantly, suggesting possible Zn dissolution. The final treatment, for 20 additional minutes, led to irregular Pd steps decorated by smaller monolayer ZnO_x islands (Figure 1f).

HREELS analysis of the surface after each treatment demonstrated that hydroxyl groups are successively removed from the surface (the full spectra are shown in Figure S2 in the Supporting Information). After the first treatment, HREELS showed a significant ν(O−D) peak at 2660 cm^{-1} in addition to a weakened ν(O−H) peak (Figure 2, red line). The centroid of the ν(O−H) peak shifts slightly toward lower frequencies. The ν(O−D) and ν(O−H) peaks get broader (fwhm = 61 and 51 cm^{-1}, respectively), pointing to an inhomogeneous chemical environment of the hydroxyl species and/or the possible formation of another hydroxylated zinc oxide phase. Indeed, on Pt(111), the ultrathin zinc oxide films demonstrated the dynamic structural transformations,[41] which might be a case for Pd(111) as well. After the second and third treatments, neither ν(O−D) nor ν(O−H) vibrations (blue line and green lines) were retained on the surface, indicating that the monolayer structure does not contain hydroxyl groups, and OH (OD) vibrations, therefore, come solely from the bilayer islands. Zn $2p_{3/2}$ XPS spectra were collected to identify the chemical states of Zn during these transformations. As shown in Figure 3a (purple line), after diethylzinc deposition and annealing in UHV, diethylzinc was completely decomposed, and Zn formed a near-surface alloy with the Pd substrate,

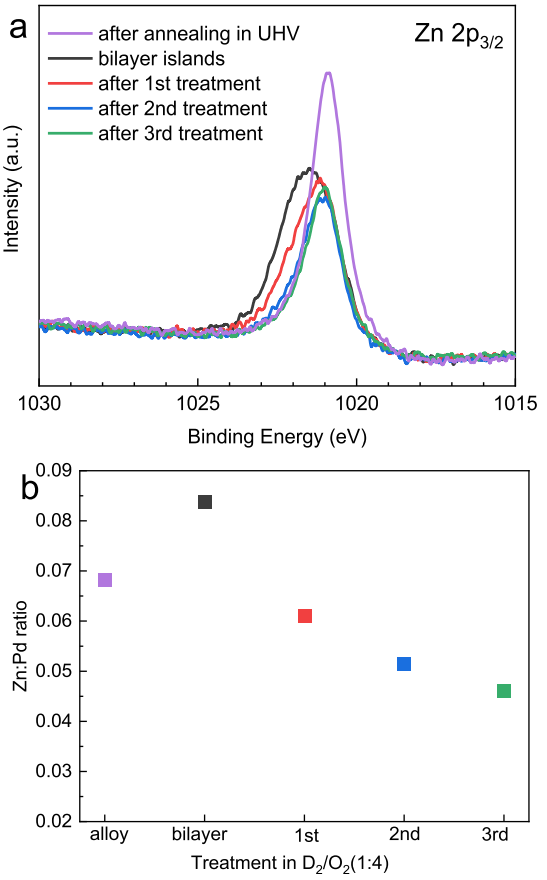

Figure 3. XPS analysis of the 0.32 ML ZnO_x/Pd(111) sample. (a) Zn $2p_{3/2}$ XPS peak of the surfaces after diethylzinc deposition and annealing in UHV, post-oxidation in 5×10^{-7} mbar of O_2 at 550 K for 10 min, and after sequential treatments in a 5×10^{-7} mbar D_2/O_2 (1:4) mixture at 550 K for 10, 10 and 20 min. (b) Zn/Pd atomic ratio of the surfaces calculated from the XPS spectra in (a).

https://doi.org/10.1021/acsami.1c07510
ACS Appl. Mater. Interfaces XXXX, XXX, XXX−XXX

showing a narrow peak at 1020.9 eV with fwhm of 1.2 eV. No carbon signal was detected. Post-oxidation in 5×10^{-7} mbar of O_2 formed bilayer ZnO islands with a broad peak centered at 1021.5 eV with a fwhm of 2.1 eV, indicating the existence of two or more Zn species in different chemical environments (black line).

After treating the surface in D_2/O_2, the peak was gradually narrowed and shifted to lower binding energies. After three D_2/O_2 treatments, the Zn $2p_{3/2}$ peak was located at 1021.0 eV with a fwhm of 1.3 eV (green line), which is very similar to the peak shown in purple and, therefore, corresponds to a Pd−Zn near-surface alloy. Zn LMM Auger peaks show corresponding changes; while, Pd 3d peaks did not show significant changes due to the large contribution of bulk Pd atoms, which are not affected. The O 1s peak is overlapped with the Pd $3p_{3/2}$ peak and thus cannot be observed in our case (Figure S3 in the Supporting Information).

The atomic ratio of Zn to Pd in the near-surface region was calculated by using the peak areas corrected on the Scofield relative sensitivity factors (Figure 3b). After the initial diethylzinc deposition and annealing in UHV, the Zn/Pd ratio was 0.060. The ratio increased to 0.084 after post-oxidation to form a bilayer ZnO. This change is related to the favorability of Zn dissolution in Pd(111);[42] once a surface Pd−Zn alloy is formed, some Zn atoms will gradually diffuse into the Pd lattice, and photoelectrons emitted from these Zn moieties will be attenuated when traveling through Pd adlayers, giving a smaller nominal Zn/Pd ratio. Subsequently, during post-oxidation, Zn will be pulled out to form bilayer ZnO islands on the surface, leading to a higher Zn/Pd ratio (similar behavior has been observed for the Pd−Al system[43]). Following the sequential D_2/O_2 treatments, the Zn/Pd ratio decreased again to 0.061, 0.051, and finally 0.046. Such decrease indicates that zinc diffused once again into the subsurface of the Pd crystal during the D_2/O_2 treatments.

In aggregate, the above results, including the smaller fwhm, lower binding energy, and smaller Zn/Pd ratio, indicate that Zn was reduced and diffused into the Pd lattice to form a near-surface Pd−Zn alloy in the D_2/O_2 (1:4) atmosphere, even in the presence of significant excess of O_2. There, bilayer ZnO islands converted to a monolayer "5Å-ZnO_x" structure and then to a near-surface Pd−Zn alloy, where the "5Å-ZnO_x" monolayer structure acts as an intermediate phase and is observed in the short time treatments. It is well known that the Pd−Zn alloys are stable under reducing conditions,[44,45] but the above results indicate that even under the O_2 and D_2 (H_2) mixture conditions, local alloy formation and further Zn dissolution are also favorable. The changes imply that alloy formation is the thermodynamic driving force of zinc oxide migration on the palladium surface in this system. It is worth noting that during the treatments in the D_2/O_2 (1:4) mixture, water may inevitably form on the surface. We studied the role of water by introducing D_2O when preparing ZnO films (Figure S8 in the Supporting Information). The formation of the same bilayer islands as those in pure O_2 and the absence of the ν(O−D) signal indicate that D_2O was not activated during the preparation and, therefore, the influence of water is negligible.

To study the reversibility of the above structure transitions, we conducted post-oxidation of the near-surface Pd−Zn alloy in a D_2/O_2 mixture, as shown in Figure 4a,b. The "5Å-ZnO_x" monolayer structure on Pd(111) with a 0.33 ML coverage was obtained in 5×10^{-7} mbar of a D_2/O_2 (4:7) mixture at 550 K for 10 min. HREELS confirmed that the monolayer structure is free of hydroxyl species (Figure 4c, full spectra shown in Figure S4 in the Supporting Information). Subsequent treatment with pure O_2 at 5×10^{-7} mbar at 550 K for 10 min led to formation of the hydroxylated bilayer islands. Therefore, the reversibility of the structure transition was confirmed. In addition, the reversible formation of the alloy phase can also be confirmed from the preparation method itself. That is, after deposition of diethylzinc and annealing in UHV, the collected Zn $2p_{3/2}$ XPS spectra show that Zn is in a metallic state; while, the O_2 treatment transforms all the alloyed/deposited Zn to bilayer ZnO. This reversible phase transition demonstrates that the zinc oxide/hydroxide film structure on Pd(111) is readily controlled by the gas-phase conditions.

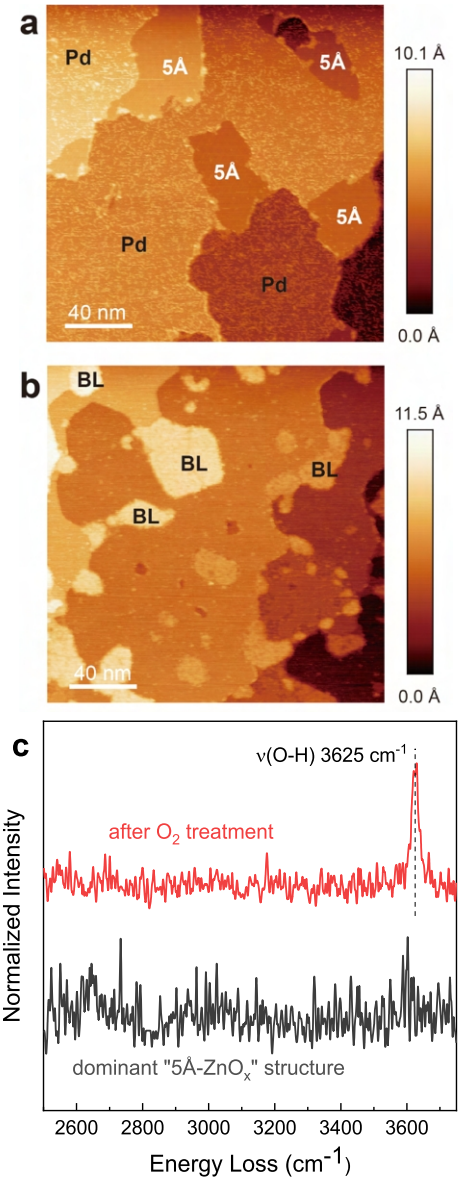

Figure 4. STM images and HREEL spectra of the 0.33 ML ZnO_x/Pd (111) sample. The size of the images is 200 × 200 nm. (a) Fresh surface prepared in a 5×10^{-7} mbar D_2/O_2 (4:7) mixture at 550 K with a dominant "5Å-ZnO_x" structure labeled as "5Å" in the image. (b) The surface after subsequent treatment in O_2 at 5×10^{-7} mbar at 550 K for 10 min (c) HREEL spectra as-prepared and after treatment in O_2.

https://doi.org/10.1021/acsami.1c07510
ACS Appl. Mater. Interfaces XXXX, XXX, XXX−XXX

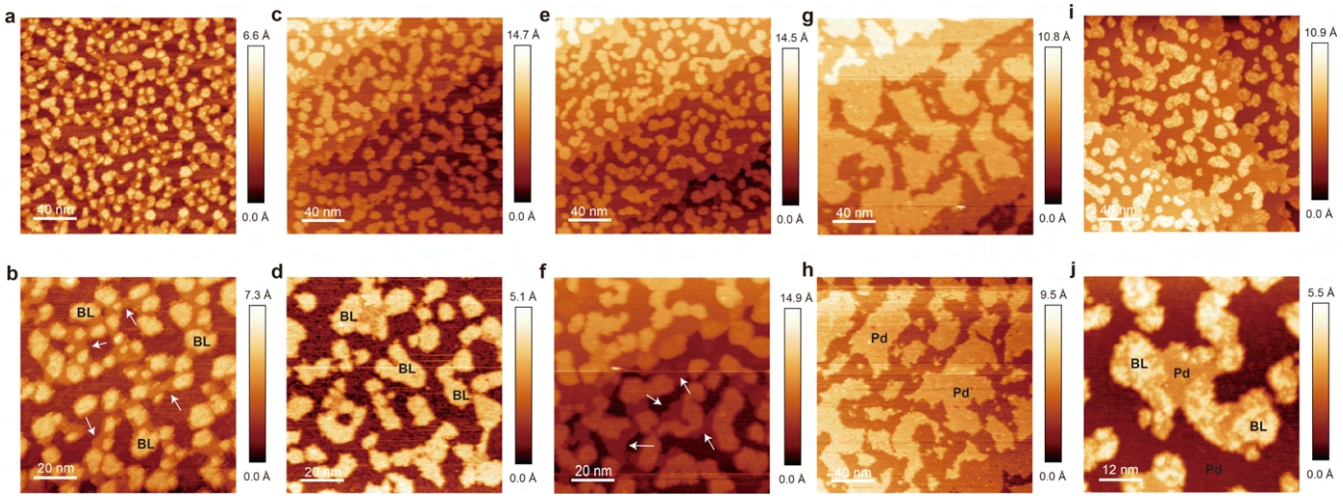

Figure 5. STM images of 0.68 ML ZnO_x/Pd(111) with the structural transformation from the bilayer islands to the Pd−Zn alloy. (a,b) Fresh 0.68 ML ZnO_x/Pd(111) surface prepared by oxidative Zn evaporation and post-oxidation in 1×10^{-6} mbar O_2 at 550 K. (c,d) Surface after the first sequential treatment in a 5×10^{-7} mbar D_2/O_2 (1:4) mixture at 550 K for 10 min. (e,f) Surface after the second treatment in 5×10^{-7} mbar D_2/O_2 (1:4) at 550 K for 20 min. (g,h) Surface after the third treatment in 5×10^{-7} mbar D_2/O_2 (4:7) at 550 K for 10 min. (i,j) Surface after fourth treatment in 5×10^{-7} mbar O_2 at 550 K for 5 min. White arrows indicate monolayer structures.

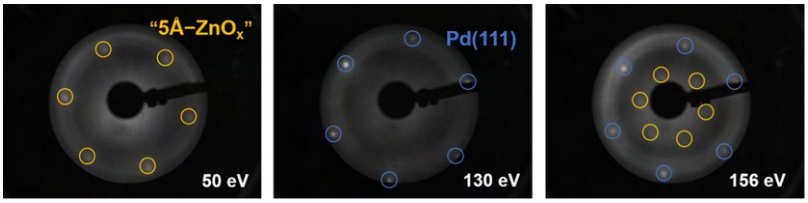

Figure 6. LEED patterns of the "5Å-ZnO_x" monolayer structure superimposed on the Pd(111) surface at different electron energies.

To study the influence of the surface coverage on the structure transition, we performed additional experiments by doubling the Zn coverage. Bilayer ZnO islands on Pd(111) with a coverage of 0.68 ML were prepared by oxidative Zn evaporation following post-oxidation in 1×10^{-6} mbar of O_2 at 550 K for 20 min (Figure 5a,b). It is worth noting that the formation of the bilayer islands is incomplete, and monolayer films were observed between bilayer islands, though atomic resolution was not achieved. Treating the sample in 5×10^{-7} mbar of a D_2/O_2 (1:4) mixture at 550 K for 10 min resulted in the disappearance of those monolayer films (Figure 5c,d); while, another treatment for 20 more minutes led to the appearance of additional monolayer films at the perimeters of the bilayer islands (Figure 5e,f). The first D_2/O_2 treatment indicated that the reduction of the monolayer is faster than the reduction of the bilayer, so the monolayer was cleaned off in the first 10 min; while, the fraction of the remaining bilayer transformed to a monolayer in the following 20 min. A third treatment in 5×10^{-7} mbar of the D_2/O_2 (4:7) mixture at 550 K for 10 min resulted in complete reduction of zinc oxide and formation of a Pd−Zn near-surface alloy, as indicated by the large Pd patches in STM images (Figure 5g,h). A re-oxidation in 5×10^{-7} mbar of O_2 at 550 K for 5 min recovered the bilayer ZnO islands with some small residual Pd patches remaining in close proximity to the newly formed bilayer ZnO (Figure 5i,j). Overall, this reversible transformation between bilayer ZnO and the Pd−Zn alloy is similar to the trend observed at low Zn coverages.

3.2. Resolving the "5Å-ZnO_x" Monolayer Structure. The "5Å-ZnO_x" monolayer phase is an important intermediate in the structure transition on Pd(111). Therefore, we employed STM, LEED, and DFT modeling to elucidate the atomic-scale details of this structure. Samples with this monolayer phase dominating the surface can be prepared by two approaches: post-oxidation in a D_2/O_2 mixture as described above or performing the transition from bilayer to alloy at 620 K with a short time to capture the intermediate phase, as shown in Figure S5 in the Supporting Information. The resulting LEED patterns show the superposition of the ZnO_x structure over the Pd(111) substrate. As shown in Figure 6, by using the Pd−Pd distance of 2.75 Å as a reference, the periodicity of ZnO_x was calculated to be 5.0 Å, which agrees well with the value measured from STM images. The ZnO reflection pattern is 30° rotated with respect to the Pd(111) pattern, corresponding to a 30° rotation of the ZnO crystallographic structure in respect to the Pd(111) substrate. In addition, the STM image in Figure 1d shows a large superlattice on the monolayer island. The periodicity of the superlattice was measured to be 49.5 Å, 18 times that of the Pd−Pd spacing, and is 20° rotated with respect to the 5Å atomic periodicity. Therefore, this "5Å-ZnO_x" structure can also be denoted as (18 × 18) R20°. To the best of our knowledge, this structure has not been reported in the literature.

As discussed above, our results show that the (18 × 18) R20° structure is an intermediate phase during the transition from bilayer ZnO to Pd−Zn near-surface alloy since it only forms in a D_2/O_2 mixture at elevated temperatures for a limited time, and this structure is resistant to hydroxylation. The distance between bright spots is 5 Å, which is not a

https://doi.org/10.1021/acsami.1c07510
ACS Appl. Mater. Interfaces XXXX, XXX, XXX−XXX

multiple of the ZnO lattice constant. This result rules out the existence of a pure ZnO phase, as the ZnO lattice constant is close to 3.25 Å. There is a 30° rotation between the direction of oxygen alignment and the Pd $\langle\bar{1}10\rangle$ direction and a 20° rotation between the large superlattice and oxygen alignment, suggesting the superlattice does not originate from the overlap of the upper ZnO_x layer and underlying Pd(111). In fact, in light of the diffusion of zinc atoms into Pd subsurface during the transition, we hypothesize that the (18 × 18) R20° phase has a Pd−Zn surface alloy as the substrate. The presence of Zn atoms within the vicinity of certain oxygen moieties changes the local density of states, which is observed by STM. We used DFT calculations to further elucidate the "5Å-ZnO_x" structure. Using simulated STM, we found a $(\sqrt{3} \times \sqrt{3})$ R30° structure, with oxygen atoms adsorbed onto threefold sites, such that the distance between them is $\sqrt{3}$ times that of the Pd−Pd distance, which is close to 5 Å (Figure 7). The simple model

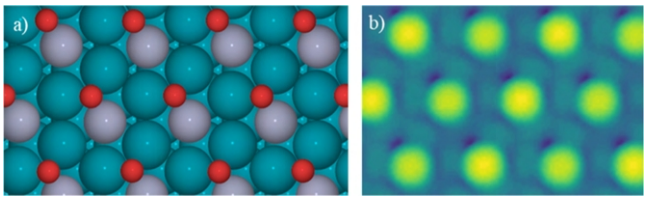

Figure 7. (a) DFT-simulated image for $(\sqrt{3} \times \sqrt{3})$ R30°, which is a proxy for the (18 × 18) R20° structure. Blue, red, and purple colors are assigned to Pd, O, and Zn, respectively. (b) Simulated STM image where the bright green spots align with oxygen atoms.

suggests that the local lean surface Zn alloys are the building blocks of this structure. In the full structure, the Zn atoms will be distributed in the surface and subsurface layers to give the actual STM pattern.

3.3. Theoretical Results. The mixed canonical method was used to plot a surface phase diagram based on the DFT calculations of all relevant surface films, as discussed in Section 3.1 (Figure 8). For clarity, only the structures closest to the thermodynamic hull and the structures relevant to the experimental observations are shown in the figure. The chemical potential of oxygen ($\Delta\mu_O$) was fixed at −1.01 eV, which corresponds to 5 × 10^{-7} mbar O_2 at 550 K, and the chemical potential of hydrogen ($\Delta\mu_H$) was fixed at −0.91 eV, corresponding to 1 × 10^{-10} mbar H_2; these conditions closely mimic the experimental gas-phase conditions. The results demonstrate that hydrogen can adsorb on the ZnO layers,[46] and the optimal hydrogen coverage on the topmost ZnO layer is 0.33 ML or one hydrogen per three surface oxygen atoms (Figure 8d). This structure may contribute to the experimentally observed ν(O−H) frequency under these conditions. DFT calculations predict the frequency to be around 3712 cm^{-1} (3716, 3713, 3708 for 3 OH in the unit cell), which is higher than the experimental observed frequency but within DFT error (~5%).[47] The ν(O−H) frequencies for OH/Pd(111) and ZnOH/Pd(111) are 3704 cm^{-1} and 3705 cm^{-1}, respectively. Therefore, the phase diagram is a more reliable tool to differentiate between these structures. The other structure on the hull is Pd(111) with adsorbed atomic O (Figure 8b). The monolayer ZnO (Figure 8c) and the surface alloys (Figure 9c) are metastable with respect to the hull, and to reach phase equilibrium, these (or other) phases will always separate to form mixtures of the bilayer ZnO and O/Pd(111) with the relative amounts determined by the initial Zn

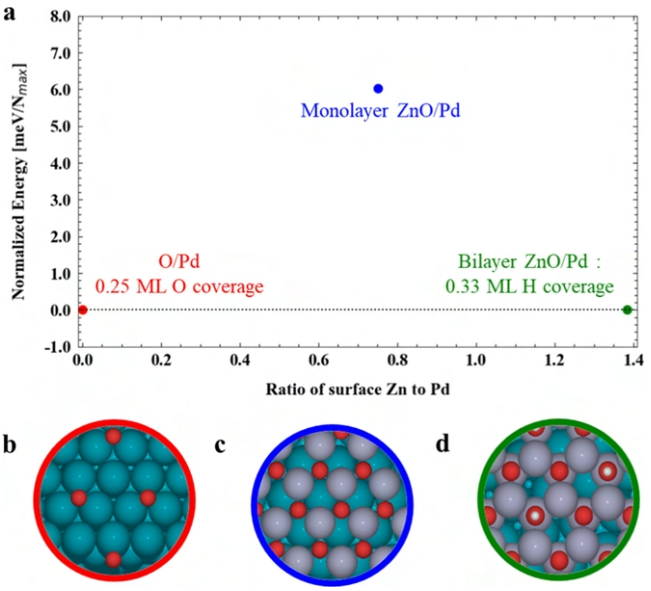

Figure 8. (a) Mixed canonical phase diagram plotted at 5 × 10^{-7}mbar of O_2 pressure. The dotted black line joining O/Pd and the bilayer ZnO with 0.33 ML H coverage is the hull line. (b) O/Pd, (c) ZnO/Pd (monolayer), and (d) $ZnOH_x$/Pd (bilayer).

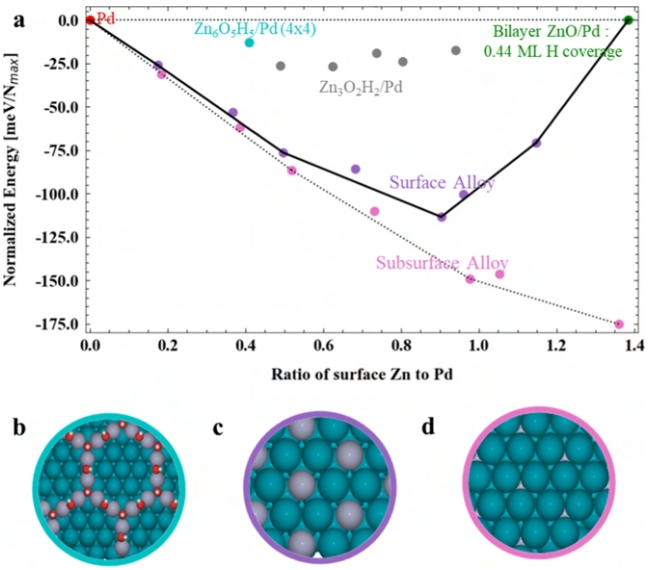

Figure 9. (a) Mixed canonical phase diagram plotted under conditions corresponding to the hydrogen treatment (10^{-7}mbar of H_2 and 10^{-10} mbar H_2O). The solid black line joining bare Pd—surface alloy—bilayer ZnO is the new hull considering only the surface structures. The dotted line shows the hull with subsurface alloys (b) $Zn_6H_5O_5$ ring structure.[17] (c) Surface Pd−Zn alloy on Pd(111) with 0.33 Zn coverage. (d) Subsurface Pd−Zn alloy on Pd(111) with 0.33 Zn coverage.

coverage. This is exactly what we see experimentally under these conditions: the deposited Zn undergoes the phase separation to form bilayer ZnO islands and bare Pd.

Introduction of hydrogen causes a shift in the surface phase diagrams. The hydrogen chemical potential ($\Delta\mu_H$) was fixed at −0.75 eV, which corresponds to 1 × 10^{-7} mbar H_2, and we assume negligible difference between H_2 and D_2 thermodynamics. The dissociation of hydrogen on bare Pd has zero barrier; while, for oxygen, the calculations predict a barrier of

https://doi.org/10.1021/acsami.1c07510
ACS Appl. Mater. Interfaces XXXX, XXX, XXX−XXX

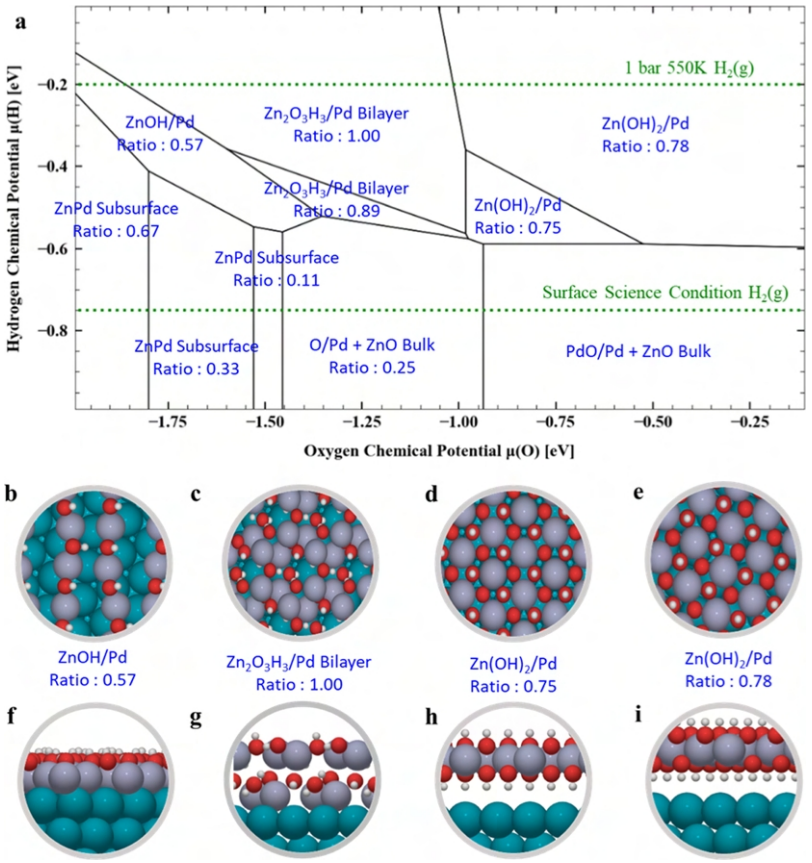

Figure 10. (a) Grand canonical phase diagram with references $H_2(g)$, $O_2(g)$, and bulk ZnO. The top dotted green line represents the chemical potential of H_2 at 1 bar, and 550 K, and the bottom dotted green line represents the experimental conditions, i.e., H_2 at 1×10^{-7} mbar, 550 K. Top and side views of (b,f) ZnOH/Pd, (c,g) $Zn_2O_3H_3$/Pd, (d,h) $Zn(OH)_2$/Pd (0.75), and (e,i) $Zn(OH)_2$/Pd (0.78) structures.

0.64 eV (Figure S12 in the Supporting Information). Therefore, we expect that the surface will be in equilibrium with gas phase hydrogen species but not necessarily with gas phase oxygen. Further, surface hydrogen atoms can rapidly react with surface oxygen and oxygen-containing species to form water (experiments demonstrate the existence of water with a partial pressure on the level of 10^{-9} mbar—Figure S6 in the Supporting Information). The surface oxygen chemical potential will, therefore, be much lower than the gas phase oxygen chemical potential since oxygen is not replenished as quickly as it is consumed to form water. The water formation equilibrium gives a lower limit for the surface oxygen chemical potential, but since the barrier for water formation on Pd(111) is 0.59 eV, equilibrium will not be achieved, and the actual chemical potential will be higher than this value. As a very simple approximation of this state, we assume the water pressure is within an order of magnitude of the hydrogen pressure, which has the effect of increasing the oxygen chemical potential to −2.52 eV. Figure 9 shows the transformed mixed canonical phase diagram after hydrogen treatment. The extrema are fixed by bare Pd and bilayer ZnO with surface H. The surface alloys drop below the hull and become thermodynamically stable (multiple possible Zn coverages were considered—Figure S10 in the Supporting Information). Further, the subsurface alloys are more stable than the surface alloys. From these observations, we conclude that Zn prefers to dissolve into the Pd lattice rather than segregate to the surface. The Pd lattice effectively acts as a Zn sink and, depending on the kinetics of the diffusion process, lean alloys of Zn will form under these conditions. These predictions are consistent with all available experimental observations.

The combined experimental and computational results present a consistent picture of the evolution of Zn-containing surface phases on Pd substrates under UHV conditions. The ability to elucidate such structures is one of the great strengths of surface science measurements. However, to assess the relevance of such measurements and the associated structures deduced from computational analysis for higher pressure conditions relevant to the classic SMSI effect, a modified thermodynamic formalism must be employed to extrapolate to real SMSI conditions. This can be accomplished by modeling the metal nanoparticle and supporting oxide, which may constitute a traditional SMSI system, as infinite reservoirs of Pd metal and ZnO in a grand canonical ensemble (Figure 10). Both hydrogen and oxygen chemical potentials are kept open, and the Zn chemical potential is referenced to the bulk ZnO support. As described above, under these conditions, bulk ZnO and O/Pd will be observed if the zinc potential is fixed by bulk ZnO. However, the hydrogen chemical potential is too low to form thermodynamically stabile ZnO_xH_y films in UHV. Under realistic SMSI conditions, though, the much higher hydrogen chemical potentials qualitatively change this picture. The green dotted line in Figure 10 is plotted at 1 bar H_2 pressure at 550 K. It is seen that, irrespective of the oxygen chemical potential, ZnO_xH_y films will form, although the particular stoichiometry is sensitive to the oxygen chemical potential. It is worth noting that certain surface stoichiometries, such as ZnOH and

https://doi.org/10.1021/acsami.1c07510
ACS Appl. Mater. Interfaces XXXX, XXX, XXX−XXX

$Zn_2O_3H_3$, that do not exist in bulk are found to be stable under these conditions. This behavior is traced to both hydrogen incorporation into the films and strong stabilization of the films by the Pd substrates. Some of the resulting structures could, in fact, have relevance for practical catalysis. For example, ZnOH/Pd (Figure 10b) is linear structure and has three phase boundary sites that can be interesting for catalysis. The $Zn_2O_3H_3$ (Figure S11 in the Supporting Information) phase also has open three phase boundary sites, but closed bilayer structures of $Zn_2O_3H_3$ (Figure 10c) are slightly more stable. The $Zn(OH)_2$ (Figure 10d,e) phase is a three-layered continuous structure, such that Zn is sandwiched between two layers of OH with H facing outward. In the methanol synthesis reaction, the H_2 pressure is generally on the order of 10 bar, and thus DFT calculations predict the formation of these hydroxylated phases. Although experimentally it is difficult to characterize these structures, Xu et al.[48] and Kast et al.[49] have reported the existence of ZnO_x islands on Pd nanoparticles under reaction conditions.

3.4. Mechanical Origin of SMSI Behavior of ZnO Films on Pd Surfaces. The inverse catalyst model of ZnO_xH_y/Pd(111) considered in this study resembles the oxide overlayer that forms on metal nanoparticle surfaces in SMSI. From the considerations described above, we propose two mechanisms by which SMSI-like effects may occur in the Pd/ZnO system. First, ZnO was observed to be atomically mobile, leading to rearrangement and formation of different phases. The newly formed phase grows from the existing phase, which suggests that ZnO species diffuse in two dimensions on the metal surface. Our experimental observations indicate that the (18 × 18) R20° structure forms as an intermediate phase during the transition from the bilayer ZnO to the near-surface alloy under D_2/O_2 conditions. Therefore, the oxide is, in fact, reduced, and zinc atoms subsequently dissolve into the palladium lattice. Zn prefers to form lean alloys with Pd, and so the first layer of ZnO, on top of surface Pd, spreads while breaking into alloys. The second mechanism involves the formation of thin ZnO_xH_y films. In this situation, the hydroxylation of the oxide results in a new hydroxyl oxide film on the metal surface with either lower or equal oxidation state to that in ZnO. Under these two circumstances, the SMSI overlayers are different. The former is a ZnO_x overlayer, which eventually transforms into a surface alloy layer; while, the latter consists of two dimensional ZnO_xH_y films, which may or may not transform into a surface alloy.

There is an open debate in the literature as to whether the overlayers on SMSI catalysts observed using microscopic and spectroscopic techniques are partially reduced oxides or bimetallic alloys.[49−53] Our results indicate that both scenarios are possible, depending on the gas-phase conditions, coverage of oxide on the metal surface, and reaction quenching to control surface chemical potentials, at least for the transition metals which can form alloys with group VIII noble metals such as Zn.

4. CONCLUSIONS

Our experimental and theoretical analysis demonstrates that ZnO can show SMSI-like behavior under weakly reducing surface science conditions (5×10^{-7} mbar of D_2/O_2 (1:4) mixture and 550 K). Aided by the use of DFT calculations and a mixed canonical−grand canonical phase diagram, the atomic-scale details of these processes are elucidated. Zinc oxide/hydroxide transforms from bilayer islands to a Pd−Zn subsurface alloy through a newly discovered (18 × 18) R20° intermediate phase, and the transformations are reversible in nature. DFT calculations further reveal that under realistic SMSI conditions, the formation of the other ZnO_xH_y intermediates is favored, which could significantly alter the catalytic behavior of ZnO supported catalysts. The aggregate results suggest that migration and spreading of ZnO on metal surfaces are found to be enabled by two different mechanisms: ZnO_xH_y intermediates formation and surface alloy formation, both of which require the presence of H_2 (D_2).

Although SMSI effects are ultimately system specific, our study serves as a template to help understand the interplay of surface structures and their energetics in a variety of systems. In particular, the two mechanisms for SMSI proposed in this work could, in theory, be applied to the interpretation of a wide variety of SMSI-related structure transformations.

■ ASSOCIATED CONTENT

Supporting Information

The Supporting Information is available free of charge at https://pubs.acs.org/doi/10.1021/acsami.1c07510.

Histogram of the apparent height of a bilayer ZnO island; wide-range HREELS spectra; Zn LMM Auger, Pd $3p_{3/2}$, and Pd 3d XPS signals; STM images of transformations at 620 K; mass spectrum collected during the transformation; STM and HREELS of the (4 × 4)-$Zn_6O_5H_5$ structure; STM and HREELS of the surface prepared in a D_2O and O_2 mixture post-oxidation; derivation of a mixed canonical model; chemical potential calculations; structures of relevant surface species; and nudged elastic band calculations (PDF)

■ AUTHOR INFORMATION

Corresponding Authors

Zhenhua Zeng − *Davidson School of Chemical Engineering, Purdue University, West Lafayette, Indiana 47906, United States*; Email: zeng46@purdue.edu

Dmitry Zemlyanov − *Birck Nanotechnology Center, Purdue University, West Lafayette, Indiana 47907, United States*; orcid.org/0000-0002-1221-9195; Email: dzemlian@purdue.edu

Jeffrey P. Greeley − *Davidson School of Chemical Engineering, Purdue University, West Lafayette, Indiana 47906, United States*; orcid.org/0000-0001-8469-1715; Email: jgreeley@purdue.edu

Authors

Junxian Gao − *Davidson School of Chemical Engineering, Purdue University, West Lafayette, Indiana 47906, United States*; orcid.org/0000-0002-1015-7103

Kaustubh J. Sawant − *Davidson School of Chemical Engineering, Purdue University, West Lafayette, Indiana 47906, United States*

Jeffrey T. Miller − *Davidson School of Chemical Engineering, Purdue University, West Lafayette, Indiana 47906, United States*; orcid.org/0000-0002-6269-0620

Complete contact information is available at: https://pubs.acs.org/10.1021/acsami.1c07510

https://doi.org/10.1021/acsami.1c07510
ACS Appl. Mater. Interfaces XXXX, XXX, XXX−XXX

Author Contributions

J.G. and K.J.S. contributed equally. The manuscript was written through contributions of all authors. All authors have given approval to the final version of the manuscript.

Notes

The authors declare no competing financial interest.

■ ACKNOWLEDGMENTS

The authors gratefully acknowledge the financial support from the National Science Foundation under award no. 1804712. The use of the Center for Nanoscale Materials (CNM), an Office of Science user facility, was supported by the U.S. Department of Energy, Office of Science, Office of Basic Energy Sciences, under contract no. DE-AC02-06CH11357. J.G. and D.Z. would like to thank Dr. Nathan Guisinger at CNM for the use of the STM tip etching tool.

■ ABBREVIATIONS

DFT, density functional theory
STM, scanning tunneling microscopy
XPS, X-ray photoelectron spectroscopy
HREELS, high-resolution electron energy loss spectroscopy
LEED, low energy electron diffraction
SMSI, strong metal−support interaction
UHV, ultrahigh vacuum
NEB, nudged elastic band

■ REFERENCES

(1) Tauster, S. J.; Fung, S. C.; Garten, R. L. Strong Metal-Support Interactions. Group 8 Noble Metals Supported on TiO_2. *J. Am. Chem. Soc.* **1978**, *100*, 170−175.
(2) Bernal, S.; Botana, F. J.; Calvino, J. J.; López, C.; Pérez-Omil, J. A.; Rodríguez-Izquierdo, J. M. High-Resolution Electron Microscopy Investigation of Metal-Support Interactions in Rh/TiO_2. *J. Chem. Soc., Faraday Trans.* **1996**, *92*, 2799−2809.
(3) Zhang, S.; Plessow, P. N.; Willis, J. J.; Dai, S.; Xu, M.; Graham, G. W.; Cargnello, M.; Abild-Pedersen, F.; Pan, X. Dynamical Observation and Detailed Description of Catalysts under Strong Metal-Support Interaction. *Nano Lett.* **2016**, *16*, 4528−4534.
(4) van Deelen, T. W.; Hernández Mejía, C.; de Jong, K. P. Control of Metal-Support Interactions in Heterogeneous Catalysts to Enhance Activity and Selectivity. *Nat. Catal.* **2019**, *2*, 955−970.
(5) Tauster, S. J. Strong metal-support interactions. *Acc. Chem. Res.* **1987**, *20*, 389−394.
(6) Pesty, F.; Steinrück, H.-P.; Madey, T. E. Thermal Stability of Pt Films on TiO_2(110): Evidence for Encapsulation. *Surf. Sci.* **1995**, *339*, 83−95.
(7) Willinger, M. G.; Zhang, W.; Bondarchuk, O.; Shaikhutdinov, S.; Freund, H.-J.; Schlögl, R. A Case of Strong Metal-Support Interactions: Combining Advanced Microscopy and Model Systems to Elucidate the Atomic Structure of Interfaces. *Angew. Chem., Int. Ed.* **2014**, *53*, 5998−6001.
(8) Suzuki, T.; Souda, R. The Encapsulation of Pd by the Supporting TiO_2(110) Surface Induced by Strong Metal-Support Interactions. *Surf. Sci.* **2000**, *448*, 33−39.
(9) Matsubu, J. C.; Zhang, S.; DeRita, L.; Marinkovic, N. S.; Chen, J. G.; Graham, G. W.; Pan, X.; Christopher, P. Adsorbate-Mediated Strong Metal-Support Interactions in Oxide-Supported Rh Catalysts. *Nat. Chem.* **2017**, *9*, 120−127.
(10) Baker, R. T. K.; Tauster, S. J.; Dumesic, J. A. Strong Metal-Support Interactions; ACS Symposium Series; American Chemical Society, 1986. DOI: 10.1021/bk-1986-0298
(11) Grunwaldt, J.-D.; Molenbroek, A. M.; Topsøe, N.-Y.; Topsøe, H.; Clausen, B. S. In Situ Investigations of Structural Changes in Cu/ZnO Catalysts. *J. Catal.* **2000**, *194*, 452−460.
(12) Naumann D'Alnoncourt, R.; Xia, X.; Strunk, J.; Löffler, E.; Hinrichsen, O.; Muhler, M. The Influence of Strongly Reducing Conditions on Strong Metal-Support Interactions in Cu/ZnO Catalysts Used for Methanol Synthesis. *Phys. Chem. Chem. Phys.* **2006**, *8*, 1525−1538.
(13) Behrens, M.; Studt, F.; Kasatkin, I.; Kühl, S.; Hävecker, M.; Abild-pedersen, F.; Zander, S.; Girgsdies, F.; Kurr, P.; Kniep, B.-L.; Tovar, M.; Fischer, R. W.; Norskov, J. K.; Schlögl, R. The Active Site of Methanol Synthesis over Cu/ZnO/Al2O3 Industrial Catalysts. *Science* **2012**, *336*, 893−897.
(14) Lunkenbein, T.; Schumann, J.; Behrens, M.; Schlögl, R.; Willinger, M. G. Formation of a ZnO Overlayer in Industrial Cu/ZnO/Al_2O_3Catalysts Induced by Strong Metal-Support Interactions. *Angew. Chem., Int. Ed.* **2015**, *54*, 4544−4548.
(15) Claeyssens, F.; Freeman, C. L.; Allan, N. L.; Sun, Y.; Ashfold, M. N. R.; Harding, J. H. Growth of ZnO thin films-experiment and theory. *J. Mater. Chem.* **2005**, *15*, 139−148.
(16) Pan, Q.; Liu, B. H.; McBriarty, M. E.; Martynova, Y.; Groot, I. M. N.; Wang, S.; Bedzyk, M. J.; Shaikhutdinov, S.; Freund, H.-J. Reactivity of Ultra-Thin ZnO Films Supported by Ag(111) and Cu(111): A Comparison to ZnO/Pt(111). *Catal. Lett.* **2014**, *144*, 648−655.
(17) Weirum, G.; Barcaro, G.; Fortunelli, A.; Weber, F.; Schennach, R.; Surnev, S.; Netzer, F. P. Growth and Surface Structure of Zinc Oxide Layers on a Pd(111) Surface. *J. Phys. Chem. C* **2010**, *114*, 15432−15439.
(18) Schott, V.; Oberhofer, H.; Birkner, A.; Xu, M.; Wang, Y.; Muhler, M.; Reuter, K.; Wöll, C. Chemical Activity of Thin Oxide Layers: Strong Interactions with the Support Yield a New Thin-Film Phase of ZnO. *Angew. Chem., Int. Ed.* **2013**, *52*, 11925−11929.
(19) Kim, C.-H.; Lee, J. S.; Trimm, D. L. The Preparation and Characterisation of Pd-ZnO Catalysts for Methanol Synthesis. *Top. Catal.* **2003**, *22*, 319−324.
(20) Iwasa, N.; Masuda, S.; Takezawa, N. Steam Reforming of Methanol over Ni, Co, Pd and Pt Supported on ZnO. *React. Kinet. Catal. Lett.* **1995**, *55*, 349−353.
(21) Chin, Y.; Dagle, R.; Hu, J.; Dohnalkova, A. C.; Wang, Y. Steam Reforming of Methanol over Highly Active Pd/ZnO Catalyst. *Catal. Today* **2002**, *77*, 79−88.
(22) Fadley, C. S. Basic Concepts of X-Ray Photoelectron Spectroscopy. *Electron Spectrosc.: Theory, Tech. Appl.* **1978**, *2*, 1−156.
(23) Paul, R.; Reifenberger, R. G.; Fisher, T. S.; Zemlyanov, D. Y. Atomic Layer Deposition of FeO on Pt(111) by Ferrocene Adsorption and Oxidation. *Chem. Mater.* **2015**, *27*, 5915−5924.
(24) Gharachorlou, A.; Detwiler, M. D.; Nartova, A. V.; Lei, Y.; Lu, J.; Elam, J. W.; Delgass, W. N.; Ribeiro, F. H.; Zemlyanov, D. Y. Palladium Nanoparticle Formation on TiO_2(110) by Thermal Decomposition of Palladium(II) Hexafluoroacetylacetonate. *ACS Appl. Mater. Interfaces* **2014**, *6*, 14702−14711.
(25) Horcas, I.; Fernández, R.; Gómez-Rodríguez, J. M.; Colchero, J.; Gómez-Herrero, J.; Baro, A. M. WSXM: A Software for Scanning Probe Microscopy and a Tool for Nanotechnology. *Rev. Sci. Instrum.* **2007**, *78*, 013705−013712.
(26) Kresse, G.; Furthmüller, J. Efficient iterative schemes forab initiototal-energy calculations using a plane-wave basis set. *Phys. Rev. B: Condens. Matter Mater. Phys.* **1996**, *54*, 11169−11186.
(27) Kresse, G.; Furthmüller, J. Efficiency of Ab-Initio Total Energy Calculations for Metals and Semiconductors Using a Plane-Wave Basis Set. *Comput. Mater. Sci.* **1996**, *6*, 15−50.
(28) Kresse, G.; Joubert, D. From Ultrasoft Pseudopotentials to the Projector Augmented-Wave Method. *Phys. Rev. B: Condens. Matter Mater. Phys.* **1999**, *59*, 1758−1775.
(29) Perdew, J. P.; Burke, K.; Ernzerhof, M. Generalized Gradient Approximation Made Simple. *Phys. Rev. Lett.* **1996**, *77*, 3865−3868.
(30) Hjorth Larsen, A.; Jørgen Mortensen, J.; Blomqvist, J.; Castelli, I. E.; Christensen, R.; Dułak, M.; Friis, J.; Groves, M. N.; Hammer, B.; Hargus, C.; Hermes, E. D.; Jennings, P. C.; Bjerre Jensen, P.; Kermode, J.; Kitchin, J. R.; Leonhard Kolsbjerg, E.; Kubal, J.; Kaasbjerg, K.; Lysgaard, S.; Bergmann Maronsson, J.; Maxson, T.;

https://doi.org/10.1021/acsami.1c07510
ACS Appl. Mater. Interfaces XXXX, XXX, XXX−XXX

Olsen, T.; Pastewka, L.; Peterson, A.; Rostgaard, C.; Schiøtz, J.; Schütt, O.; Strange, M.; Thygesen, K. S.; Vegge, T.; Vilhelmsen, L.; Walter, M.; Zeng, Z.; Jacobsen, K. W. The Atomic Simulation Environment - A Python Library for Working with Atoms. *J. Phys.: Condens. Matter* **2017**, *29*, 273002−273031.
(31) Mortensen, J.; Hansen, L.; Jacobsen, K. W. Real-Space Grid Implementation of the Projector Augmented Wave Method. *Phys. Rev. B: Condens. Matter Mater. Phys.* **2005**, *71*, 035109−035119.
(32) Armbrüster, M.; Behrens, M.; Föttinger, K.; Friedrich, M.; Gaudry, É.; Matam, S. K.; Sharma, H. R. The Intermetallic Compound ZnPd and Its Role in Methanol Steam Reforming. *Catal. Rev. - Sci. Eng.* **2013**, *55*, 289−367.
(33) Todorova, M.; Reuter, K.; Scheffler, M. Density-Functional Theory Study of the Initial Oxygen Incorporation in Pd(111). *Phys. Rev. B: Condens. Matter Mater. Phys.* **2005**, *71*, 195403.
(34) Gabasch, H.; Unterberger, W.; Hayek, K.; Klötzer, B.; Kleimenov, E.; Teschner, D.; Zafeiratos, S.; Hävecker, M.; Knop-Gericke, A.; Schlögl, R.; Han, J.; Ribeiro, F. H.; Aszalos-Kiss, B.; Curtin, T.; Zemlyanov, D. In Situ XPS Study of Pd(111) Oxidation at Elevated Pressure, Part 2: Palladium Oxidation in the 10^{-1} mbar Range. *Surf. Sci.* **2006**, *600*, 2980−2989.
(35) Han, J.; Zemlyanov, D. Y.; Ribeiro, F. H. Catalytic Combustion of Methane on Palladium Single Crystals. *Catal. Today* **2006**, *117*, 506−513.
(36) Zemlyanov, D.; Aszalos-Kiss, B.; Kleimenov, E.; Teschner, D.; Zafeiratos, S.; Hävecker, M.; Knop-Gericke, A.; Schlögl, R.; Gabasch, H.; Unterberger, W.; Hayek, K.; Klötzer, B. In Situ XPS Study of Pd(1 1 1) Oxidation. Part 1: 2D Oxide Formation in 10^{-3} mbar O_2. *Surf. Sci.* **2006**, *600*, 983−994.
(37) Zeng, Z.; Chang, K. C.; Kubal, J.; Markovic, N. M.; Greeley, J. Stabilization of Ultrathin (Hydroxy)Oxide Films on Transition Metal Substrates for Electrochemical Energy Conversion. *Nat. Energy* **2017**, *2*, 17070.
(38) Reuter, K.; Scheffler, M. First-Principles Atomistic Thermodynamics for Oxidation Catalysis: Surface Phase Diagrams and Catalytically Interesting Regions. *Phys. Rev. Lett.* **2003**, *90*, 046103−046106.
(39) Liu, B.-H.; Boscoboinik, J. A.; Cui, Y.; Shaikhutdinov, S.; Freund, H.-J. Stabilization of Ultrathin Zinc Oxide Films on Metals: Reconstruction versus Hydroxylation. *J. Phys. Chem. C* **2015**, *119*, 7842−7847.
(40) Engel, T.; Kuipers, H. A Molecular-Beam Investigation of the Scattering, Adsorption and Absorption of H_2 and D_2 from/on/in Pd(111). *Surf. Sci.* **1979**, *90*, 162−180.
(41) Liu, B.-H.; McBriarty, M. E.; Bedzyk, M. J.; Shaikhutdinov, S.; Freund, H.-J. Structural Transformations of Zinc Oxide Layers on Pt(111). *J. Phys. Chem. C* **2014**, *118*, 28725−28729.
(42) Stadlmayr, W.; Rameshan, C.; Weilach, C.; Lorenz, H.; Hävecker, M.; Blume, R.; Rocha, T.; Teschner, D.; Knop-Gericke, A.; Zemlyanov, D.; Penner, S.; Schlögl, R.; Rupprechter, G.; Klötzer, B.; Memmel, N. Temperature-Induced Modifications of PdZn Layers on Pd(111). *J. Phys. Chem. C* **2010**, *114*, 10850−10856.
(43) Gharachorlou, A.; Detwiler, M. D.; Mayr, L.; Gu, X.-K.; Greeley, J.; Reifenberger, R. G.; Delgass, W. N.; Ribeiro, F. H.; Zemlyanov, D. Y. Surface Chemistry of Trimethylaluminum on Pd(111) and Pt(111). *J. Phys. Chem. C* **2015**, *119*, 19059−19072.
(44) Chen, Z. X.; Neyman, K. M.; Gordienko, A. B.; Rösch, N. Surface Structure and Stability of PdZn and PtZn Alloys: Density-Functional Slab Model Studies. *Phys. Rev. B: Condens. Matter Mater. Phys.* **2003**, *68*, 075417.
(45) Bayer, A.; Flechtner, K.; Denecke, R.; Steinrück, H.-P.; Neyman, K. M.; Rösch, N. Electronic Properties of Thin Zn Layers on Pd(111) during Growth and Alloying. *Surf. Sci.* **2006**, *600*, 78−94.
(46) Thang, H. V.; Pacchioni, G. H_2 Adsorption on Wurtzite ZnO and on ZnO/M(111) (M=Cu, Ag and Au) Bilayer Films. *ChemNanoMat* **2019**, *5*, 932−939.
(47) Greeley, J.; Nørskov, J. K.; Mavrikakis, M. Electronic Structure and Catalysis on Metal Surfaces. *Annu. Rev. Phys. Chem.* **2002**, *53*, 319−348.
(48) Xu, J.; Su, X.; Liu, X.; Pan, X.; Pei, G.; Huang, Y.; Wang, X.; Zhang, T.; Geng, H. Methanol Synthesis from CO2 and H2 over Pd/ZnO/Al_2O_3: Catalyst Structure Dependence of Methanol Selectivity. *Appl. Catal., A* **2016**, *514*, 51−59.
(49) Kast, P.; Friedrich, M.; Girgsdies, F.; Kröhnert, J.; Teschner, D.; Lunkenbein, T.; Behrens, M.; Schlögl, R. Strong Metal-Support Interaction and Alloying in Pd/ZnO Catalysts for CO Oxidation. *Catal. Today* **2016**, *260*, 21−31.
(50) Resasco, D. E.; Weber, R. S.; Sakellson, S.; McMillan, M.; Haller, G. L. X-Ray Absorption near-Edge Structure Evidence for Direct Metal-Metal Bonding and Electron Transfer in Reduced Rh/TiO_2 Catalysts. *J. Phys. Chem.* **1988**, *92*, 189−193.
(51) Boccuzzi, F.; Chiorino, A.; Ghiotti, G. IR Study of the CO Adsorption on Pt/ZnO Samples: Evidence for a PtZn Phase Formation in the SMSI State. *Surf. Sci.* **1989**, *209*, 77−88.
(52) Zhu Chen, J.; Gao, J.; Probus, P. R.; Liu, W.; Wu, X.; Wegener, E. C.; Kropf, A. J.; Zemlyanov, D.; Zhang, G.; Yang, X.; Miller, J. T. The Effect of Strong Metal-Support Interaction (SMSI) on Pt-Ti/SiO_2 and Pt-Nb/SiO_2 catalysts for Propane Dehydrogenation. *Catal. Sci. Technol.* **2020**, *10*, 5973−5982.
(53) Beck, A.; Huang, X.; Artiglia, L.; Zabilskiy, M.; Wang, X.; Rzepka, P.; Palagin, D.; Willinger, M. G.; van Bokhoven, J. A. The Dynamics of Overlayer Formation on Catalyst Nanoparticles and Strong Metal-Support Interaction. *Nat. Commun.* **2020**, *11*, 3220.

https://doi.org/10.1021/acsami.1c07510
ACS Appl. Mater. Interfaces XXXX, XXX, XXX−XXX